Enhancement of heat and mass transfer by herringbone microstructures in a simple shear flow

Yanxing Wang[1,*], Hui Wan[2], Tie Wei[3], John Abraham[4]

[1]*Department of Mechanical and Aerospace Engineering, New Mexico State University, Las Cruces, NM 88011, USA*
[2] *Department of Mechanical and Aerospace Engineering, University of Colorado Colorado Springs, Colorado Springs, CO 80918, USA*
[3] *Department of Mechanical Engineering, New Mexico Institute of Mining and Technology, Socorro, NM 87801, USA*
[4]*Department of Mechanical Engineering, University of St. Thomas, St. Paul, MN 55105, USA*

Abstract

The heat and mass transfer characteristics of a simple shear flow over a surface covered with staggered herringbone structures are numerically investigated using the lattice Boltzmann method. Two flow motions are identified. The first is a spiral flow oscillation above the herringbone structures that advects heat and mass from the top plane to herringbone structures. The second is a flow recirculation in the grooves between the ridges that advects heat and mass from the area around the tips of the structures to their side walls and the bottom surfaces. These two basic flow motions couple together to form a complex transport mechanism. The results show that when advective heat and mass transfer takes effect at relatively large Reynolds and Schmidt numbers, the dependence of the total transfer rate on Schmidt number follows a power law, with the exponent being the same as that in the Dittus-Boelter equation for turbulent heat transfer. As Reynolds number increases, the dependence of the total transfer rate on Reynolds number also approaches a power law, and the exponent is close to that in the Dittus-Boelter equation.

1. Introduction

* Corresponding author.
Email: yxwang@nmsu.edu

Microfluidics have been the subject of considerable attention in recent decades with the development of micro fabrication technologies, and they have been widely used in fundamental and applied studies of physical, chemical, and biological processes.[1-3] In micro channels, due to their small scale, the flow is highly laminar, and diffusion is usually the primary mechanism for species transport and mixing. This diffusion takes place on much longer length and time scales than does convection. Embedded micro-structures on the surface of micro-channels can be used, however, to generate transverse flow, and chaotic advection can be produced. The transverse flow advects dissolved substances over the cross section and significantly enhances mixing and transport efficiency.[4, 5] One of the most efficient chaotic micromixers is the Staggered Herringbone Mixer (SHM) developed by Stroock et al.[4] Repeated patterns of grooves on the inner surface of the SHM create helical motion of the fluid in the microchannels, providing a mixing and transport mechanism through transversal advection.

Due to the simple fabrication and high mixing efficiency of the SHM, numerous studies have been conducted on it, including analysis of the geometric effects on mixing efficiency,[6-8] the design and optimization of micro-mixers for different applications,[9-13] and development of new designs for specific applications.[14, 15] Most of these studies, however, focus on the mixing of two species in T-type SHM mixers; in this configuration, two flows containing different species enter the mixer through two inlet branches in a T shape,[16] generating a helical pattern of flow. Several studies have shown that SHM can significantly enhance convective and boiling heat transfer inside microchannels.[17, 18] The results of these studies suggest that transverse advection generated in SHM mixer flows might enhance heat and mass transport between the bulk flow and the bottom wall. This promising mechanism might have broad applications in compact heat exchangers and microelectromechanical systems (MEMS), and could also be extended to chemistry, biology, and

areas involving micro-scale mass transfer. Surprisingly, the heat and mass transfer capacity of herringbone-inspired microstructures have gained little attention to date.

In a micro-channel embedded with staggered herringbone structures, a boundary layer with reduced velocity components and a helical flow pattern is developed over the structures. The generation of the helical flow pattern is directly related to the shear rate and thickness of the boundary layer. In this study, we consider a fully developed simple shear flow confined by two infinitely large planes with staggered herringbone structures embedded on the lower surface. With lattice Boltzmann method, the heat and mass transfer from the top plane to the bottom plane are numerically investigated. This study aims to identify the mechanisms for the enhancement of heat and mass transfer by the transverse flow advection over the staggered herringbone structures. This study also investigates the dependence of transfer efficiency on the influencing parameters, such as shear rate, Prandtl number, and Schmidt number. The rest of the paper is organized as follows. A detailed description of the physical model is presented in Section 2. The numerical method is described in Section 3. The results are analyzed in Section 4, and concluding remarks are made in Section 5.

2. Physical Model

As shown in Fig. 1, we model a laminar incompressible simple shear flow enclosed by two infinitely large parallel planes, with staggered herringbone structures embedded on the bottom plane. To generate a simple shear flow, the top plane moves at a constant velocity U_0, and the bottom plane is fixed. The distance between the two planes, H, is three times the height of the herringbone ridges, h. The width of the herringbone ridges, *w,* is half of h, and the spacing between neighboring ridges δ is the same as h. The angle between the ridges and the streamwise axis, θ, is

fixed at 45°. The regular arrangement of the ridges forms the periodicity of the surface geometry in both the streamwise and spanwise directions. The streamwise dimension of each unit containing a complete herringbone element can be calculated as $L_x = (\delta + w)/sin\theta$. The spanwise dimension of each unit L_y is $2L_x$. With these geometric specifications, the flow evolution is exclusively determined by the shear Reynolds number defined based on the effective shear rate S and the flow passage height $H - h$. The effective shear rate is defined as:

$$S \equiv \frac{U_0}{H-h} \tag{1}$$

and the shear Reynolds number is defined as

$$Re_S \equiv \frac{S(H-h)^2}{v} \tag{2}$$

where v is the kinematic viscosity of the working fluid. In this study, the shear Reynolds number ranges from 20 to 200. Below that range, the diffusive transfer plays a dominant role.

We seek to develop a general understanding of the enhancement of heat and mass transfer induced by herringbone structures, so the shear Reynolds numbers considered here are higher than those usual in microfluidic systems. In this study, the temperature and the concentration of dissolved species are modeled as passive scalars, released at the top plane and absorbed at both the bottom plane and the surfaces of herringbone ridges. For purposes of generalization, a nondimensional scalar concentration is utilized, which is fixed at 1 at the top plane and 0 at the bottom plane and the surfaces of herringbone ridges. The Schmidt number for scalar diffusion in this study ranges from 1 to 50. The characteristics of scalar transfer from top plane to bottom surfaces are investigated in both diffusion-dominant and advection-dominant ranges.

The height of the herringbone ridges h and the velocity of top plane U_0 are used as the characteristic length and velocity to normalize the spatial coordinates and flow velocity,

$$\tilde{x} = x/h, \tag{3}$$

$$\tilde{\mathbf{u}} = \mathbf{u}/U_0, \tag{4}$$

In normalized form, the height of the herringbone ridges is $\tilde{h} = 1$ and the velocity of the upper plane is $\widetilde{U}_0 = 1$.

3. Numerical Methods

The lattice-Boltzmann method (LBM) has particular advantages in its ability to handle, with relative ease, complex boundaries with heat and mass transfer. In this study we develop a 3-D numerical model based on the LBM to model continuum-level meso- and micro-scale incompressible fluid flow in contact with complex surface geometries. A well-established tool, LBM has been widely used to study the fluid dynamics on surfaces with complex structures.[19] LBM is well suited to the present problem because of its powerful capability in dealing with complex geometries and its high parallelizability. The dependent variable is the particle distribution function $f_\alpha(\mathbf{x}, t)$, which quantifies the probability of finding an ensemble of molecules at position $\mathbf{x}$ with velocity $\mathbf{e}_\alpha$ at time t.[20-24] In three dimensions, the velocity vector $\mathbf{e}$ can be discretized into 15, 19 or 27 components (referred to as D3Q15, D3Q19 and D3Q27).[20] Here we apply the D3Q15 approach, primarily to minimize computational load, with the recognition that the Reynolds number is relatively low.

The Boltzmann equation discretized on a lattice with the BGK form of collision operator is given for single-phase flow by Chen and Doolen,[21] Lallemand and Luo,[25, 26] and Wang et al.,[22]

$$f_\alpha(\mathbf{x}+\mathbf{e}_\alpha\delta_t, t+\delta_t) - f_\alpha(\mathbf{x},t) = -\frac{1}{\tau}\left(f_\alpha(\mathbf{x},t) - f_\alpha^{eq}(\mathbf{x},t)\right) \quad (5)$$

where $\mathbf{e}_\alpha$ is the elementary velocity vector in direction α , τ is the relaxation time, and f_α^{eq} is the equilibrium distribution function in direction α.

$$f_\alpha^{eq}(\mathbf{x},t) = w_\alpha\rho\left(1 + \frac{\mathbf{e}_\alpha\cdot\mathbf{u}}{c_S^2} + \frac{(\mathbf{e}_\alpha\cdot\mathbf{u})^2}{2c_S^4} - \frac{\mathbf{u}\cdot\mathbf{u}}{2c_S^2}\right) \quad (6)$$

The symbol w_α is the weighting coefficient, c_s is the sound speed in the lattice, and $\mathbf{u}$ is the fluid velocity. The right-hand side of Eq. (5) describes the mixing, or collision of molecules, that locally drives the flow to an equilibrium particle distribution, $f_\alpha^{eq}(\mathbf{x},t)$. Macroscopic variables such as density ρ and velocity $\mathbf{u}$ are calculated from the moments of the distribution functions,

$$\rho(\mathbf{x},t) = \sum_\alpha f_\alpha(\mathbf{x},t), \qquad \rho(\mathbf{x},t)\mathbf{u}(\mathbf{x},t) = \sum_\alpha f_\alpha(\mathbf{x},t)\mathbf{e}_\alpha \quad (7)$$

As is common, we apply the BGK model for this collision process, through which the distribution functions $f_\alpha(\mathbf{x},t)$ relax toward $f_\alpha^{eq}(\mathbf{x},t)$ with a single lattice relaxation time scale,

$$\tau = (6\nu/(c\delta x) + 1)/2 \qquad \text{and} \qquad c = \delta x/\delta t. \quad (8)$$

In the traditional treatment of solid boundaries, a solid wall is assumed to be located half way between the lattice nodes, and molecules traveling toward the wall are bounced back at the wall and return to the same node. Consequently, the distribution function in the left direction is the same as that in the right direction before streaming. The accuracy of this scheme is only 1st order. In the present study, we use the 2nd order accurate scheme proposed by Lallemand and Luo.[23] This scheme is based on a simple bounce-back treatment and interpolations. If the distance from the first fluid node to the solid boundary, q, is less than half the lattice space, the computational quantities are interpolated before propagation and bounce-back collision. If q is greater than the half-lattice space, interpolation is conducted after propagation and bounce-back collision. The

momentum exerted by the moving boundary is treated as an extra term in the bounce-back distribution function.

The moment propagation method developed by Frenkel and Ernst,[27] Lowe and Frenkel,[28] and Merks et al.[29] is used to solve for temperature. In this method, a scalar quantity T is released in the lattice and a scalar concentration field variable is propagated at the continuum level for each scalar using the particle distribution function $f_\alpha(\mathbf{x}, t)$.

$$T(\mathbf{x}, t+\delta t) = \sum_\alpha P_\alpha(\mathbf{x} - \mathbf{e}_\alpha \delta t, t+\delta t) + \Lambda T(\mathbf{x}, t) \tag{9}$$

where

$$P_\alpha(\mathbf{x} - \mathbf{e}_\alpha \delta t, t+\delta t) = \left[\frac{\hat{f}_\alpha(\mathbf{x}-\mathbf{e}_\alpha \delta t, t_+)}{\rho(\mathbf{x}-\mathbf{e}_\alpha \delta t, t)} - w_\alpha \Lambda\right] T(\mathbf{x} - \mathbf{e}_\alpha \delta t, t) \tag{10}$$

$\hat{f}_\alpha(\mathbf{x} - \mathbf{e}_\alpha \delta t, t_+)$ is the distribution function of post-collision but before-streaming, which transports scalar from the neighboring nodes $\mathbf{x} - \mathbf{e}_\alpha \delta t$ to the node $\mathbf{x}$ between t and $t + \delta t$, and

$$\Lambda = 1 - 6\,\varepsilon / c\delta x \tag{11}$$

and ε is the scalar diffusivity.

We first ran the simulation over 5 structural elements in the streamwise direction with cases with $Re_S = 200$. The results demonstrated that the spatial periodicity of flow pattern is the same as the streamwise length of the structural element. Therefore, in the subsequent large-scale study we only simulate the flow within the cuboid domain including one structural element (indicated by dashed lines in Fig. 1(b)). Periodic conditions are used in the streamwise and spanwise directions. The total number of computational grid cells is $100 \times 200 \times 140$, and 24 grid cells are used to resolve the thickness of the herringbone ridge. The computational domain is decomposed

into 56 subdomains. The Message Passing Interface (MPI) technique is used to enable parallel computing. Analysis is conducted when the flow has reached steady state.

The LBM solver has been extensively validated in previous studies, as described in Wang et al.[22, 30-32] For the present study, we also consider heat transfer in a lid-driven cavity flow in a cube with side length L as a further validation. The lid moves at a constant velocity, U_{lid}. Temperature is fixed at T_{lid} on the moving lid and at 0 on the side and bottom walls. Two governing nondimensional parameters are the Reynolds number Re_{cavity} defined as $Re_{cavity} \equiv U_{lid}L/\nu$, where ν is the kinetic viscosity of the fluid and the Prandtl number Pr is defined as $Pr \equiv \nu/\alpha$, where α is thermal diffusivity. The case with $Re_{cavity} = 1$ and $Pr = 1$ are simulated with both the present LBM solver and the open-source code Gerris.[33,34] The grid dimensions are $100 \times 100 \times 100$ in both simulations. Figure 2 shows a comparison of the normalized vertical velocity ($\tilde{u}_z \equiv u_z/U_{lid}$) and temperature ($\tilde{\phi} \equiv T/T_{lid}$) on the middle xz plane and along the central streamwise axis. The two results are in good agreement, with a maximum relative error of 3% for point-to-point comparisons for velocity and temperature.

To examine the grid sensitivity of the results, simulations were conducted with two grids of different resolutions. The number of grid points over one ridge thickness of the herringbone structures is 24 and 36, respectively. Figure 3 shows the profiles of the horizontally averaged streamwise velocity and scalar concentration for $Re_S = 200$ and $Sc = 50$, respectively. Excellent agreement between the coarse and fine grid is obtained; the maximum deviation between the two grids is less than 2%. The present results were obtained, therefore, using the coarse grid.

4. Results and Discussion

Scalar transport from the top plane to the bottom plane relies on both diffusion and the advection induced by the herringbone structures, and advective transport is dominant when the Reynolds and Schmidt numbers are large. Our focus is on the identification of the mechanisms for the enhancement of scalar transfer by herringbone structures. $Re_S = 200$ was selected as a prototypical example to analyze the flow behavior and scalar transfer characteristics.

Figure 4 shows the patterns of flow characteristics for $Re_S = 200$. Taking advantage of the periodicities in the streamwise and spanwise directions, only the flow within the cuboid domain including a single structural element was simulated. The patterns containing multiple elements shown in the figure were generated by concatenating the results from the simulation of a single element. Typical streamlines over herringbone structures are shown in Fig. 4(a). In the steady state, the streamlines coincide with the trajectories of fluid particles, illustrating the path of scalar transport by flow advection. The color represents the level of scalar concentration at $Sc = 50$. The red and blue colors indicate higher and lower concentrations, respectively. The streamline pattern shows how the flow transports a scalar from the bulk flow to the surfaces in the herringbone grooves for absorption: The fluid with higher scalar concentration flows downward in the area above the streamwise rows of backward groove tips (BGT). Then the flow is entrapped in the grooves at the BGT, and recirculates within the grooves. At the forward groove tips (FGT) the fluid flows upward and leaves the groove with lower scalar concentration. This flow motion provides the fluid contact with the surfaces of the herringbone ridges and the bottom surface between ridges, and enhances the heat and mass exchange between the bulk flow and the surface geometry.

Figure 4(b) shows iso-surfaces of the vertical velocity at $\tilde{u}_z = \pm 0.005$. Since the flow is disturbed in the lower region, the magnitude of $\tilde{u}_z$ is larger than in the upper region. As shown in

the figure, a region with negative $\tilde{u}_z$ is generated above every BGT and a region with positive $\tilde{u}_z$ is generated above every FGT. The iso-surfaces of $\tilde{u}_z$ are consistent with the streamline patterns in Fig. 4(a). Figure 4(c) shows the corresponding 2D iso-contours of vertical velocity averaged over the streamwise coordinate, $\langle \tilde{u}_z \rangle_x$ on the cross section ($(\tilde{y}, \tilde{z})$ plane). The variable averaged over the streamwise coordinate is defined as

$$\langle \tilde{\alpha} \rangle_x (\tilde{y}, \tilde{z}) \equiv \frac{1}{\tilde{L}_x} \int_{\tilde{L}_x} \tilde{\alpha}(\tilde{x}, \tilde{y}, \tilde{z}) d\tilde{x} \tag{12}$$

where $\tilde{\alpha}(\tilde{x}, \tilde{y}, \tilde{z})$ is the variable of interest, and $\tilde{L}_x$ is the length of a complete herringbone element in the streamwise direction. The iso-surfaces of $\tilde{u}_z$ in Fig. 4(b) and iso-contours of $\langle \tilde{u}_z \rangle_x$ in Fig. 4(c) describe the patterns of vertical velocity of the fluid that has been disturbed by the herringbone structures. Compared with the velocity at the top plane, the vertical velocity around the herringbone structures is much smaller. This implies that the pitch of the helix is much larger than the height of flow passage ($H - h$). It is well known that each unit of staggered herringbone structures generates a pair of counter-rotating tubular eddies extending in the streamwise direction in the upper region, and the fluid particle flows along a helical trajectory in the tubular eddies.[2, 4] The helical pattern can be inferred from the 2D streamlines, based on the streamwise averaged velocity components, $\langle \tilde{u}_y \rangle_x$ and $\langle \tilde{u}_z \rangle_x$, as shown in Fig. 4(d). The closed streamlines define the recirculating motions in the $(\tilde{y}, \tilde{z})$ plane of the helix. This continuous upward and downward flow motion enhances the scalar transport in the vertical direction.

To quantitatively compare the flow characteristics under different conditions, we define the horizontally averaged quantities as,

$$\langle \tilde{\beta} \rangle (\tilde{z}) \equiv \frac{1}{A} \int_A \tilde{\beta}(\tilde{x}, \tilde{y}, \tilde{z}) d\tilde{x} d\tilde{y} \tag{13}$$

where $\tilde{\beta}(\tilde{x},\tilde{y},\tilde{z})$ is the quantity of interest that varies with spatial coordinates and A is the horizontal area occupied by fluid at different vertical locations on a herringbone element. The averaged variable $\langle\tilde{\beta}\rangle$ is a function of the vertical coordinate $\tilde{z}$ only. The horizontally averaged vertical velocity $\langle\tilde{u}_z\rangle$ represents the net flux of fluid (flow per unit area) through the horizontal plane. As a result of mass conservation, $\langle\tilde{u}_z\rangle$ is zero for the present problem. To quantify the wall-normal advective transfer capability, we define the effective upward and downward velocity as

$$\tilde{u}_z^+ \equiv \begin{cases} \tilde{u}_z, & if\ \tilde{u}_z > 0 \\ 0, & if\ \tilde{u}_z < 0 \end{cases} \quad \text{and} \quad \tilde{u}_z^- \equiv \begin{cases} 0, & if\ \tilde{u}_z > 0 \\ \tilde{u}_z, & if\ \tilde{u}_z < 0 \end{cases} \tag{14}$$

In this study, we use $\tilde{u}_z^-$ to deal with the heat and mass transfer from the bulk flow to the bottom surface.

Figure 5 plots the profiles of horizontally averaged streamwise velocity $\langle\tilde{u}_x\rangle$ and the effective downward velocity $\langle\tilde{u}_z^-\rangle$ at $Re_S = 20$ and 200. The horizontal dashed line indicates the height of the herringbone structures. The curves of $\langle\tilde{u}_x\rangle$ shows little difference between $Re_S = 20$ and 200, decreasing roughly linearly above the ridge tips ($\tilde{u} > 1$), from 1 at the upper plane to a small value close to 0 at the ridge tips. In the grooves ($\tilde{u} < 1$), $\langle\tilde{u}_x\rangle$ remains small. The roughly linear variation of $\langle\tilde{u}_x\rangle$ above the grooves suggests that the resistance of the herringbone structures is close to that of a smooth plane. The effective resistance of the herringbone structures is related to both structure geometry and fluid behavior. That is, the gaps between the ridges decrease the horizontal wall area at ridge-tip height, and so decrease the resistance, yet the vertical flow advection (Fig. 4) increases the flow shear stress on the top surfaces of the ridges. For larger Reynolds numbers, this increase is larger. In steady state, the resistance caused by the herringbone structures is the same as the shear force on the tops of the ridges. For the present geometry, the

ratio of the resistance over the herringbone structures to that over smooth plane at ridge-tip height is 0.97 and 1.02 for $Re_S = 20$ and 200, respectively.

The effective downward velocity $\langle \tilde{u}_z^- \rangle$ curves (Fig. 5b) are different for $Re_S = 20$ and 200, which suggests that the influence of Reynolds number primarily occurs with the vertical velocity component. The curves of $\langle \tilde{u}_z^- \rangle$ have two peaks, one above the herringbone ridge tips and the other below, corresponding to the consecutive upward and downward flow motions in the helix in the upper region and the flow recirculation in the grooves, respectively. Close to the herringbone structures, the velocity magnitude is larger, so the upper peak is close to the herringbone tips. The magnitude of $\langle \tilde{u}_z^- \rangle$ largely indicates the advective scalar transport capability of the two flows. As shown in the figure, the value of $|\langle \tilde{u}_z^- \rangle|$ for $Re_S = 20$ is larger at the upper peak and smaller at the lower peak, suggesting that the upper bulk flow at $Re_S = 20$ has greater capability for scalar transport to the herringbone top surfaces and to the recirculating flow in the grooves.

In the grooves, the situation is just the opposite. The flow at $Re_S = 200$ shows greater capability for scalar transport to the bottom surface than the flow at $Re_S = 20$. This is because the flow recirculation in the grooves is more active at larger Reynolds numbers, while at smaller Reynolds number the greater viscous effect in the upper region enables the disturbance from the herringbone structures to propagate further downstream. The overall heat and mass transfer process depends on the coupling of these two mechanisms through a complex relationship, but generally the flows at larger Reynolds numbers have a stronger advective scalar transport capability.

Scalar transport also depends on Schmidt number. For heat transfer, the corresponding characteristic number is the Prandtl number. Here we use the flow at $Re_S = 200$ to analyze the

effect of the Schmidt number. Figure 6 shows the patterns of scalar concentration for $Sc = 1$ and 50. At $Sc = 1$, the diffusion effect is so strong that the diffusive scalar transport dominates the advective scalar transport. The 3D iso-surfaces and 2D contours on two typical cross sections shown in Fig. 6(a) suggest that the scalar concentration ϕ changes roughly linearly with the vertical coordinate in the flow above the herringbone structure. The herringbone ridges cause only a slight disturbance to the distribution of ϕ. In the grooves, ϕ is low. This pattern means that the majority of the scalar is absorbed at the top surface. Further, the advection of the recirculating flow is the primary means for scalar transport in the grooves, and the reduced advective scalar transport of the recirculating flow at lower Sc cannot effectively transport a scalar to the bottom surfaces in the grooves.

At $Sc = 50$, the diffusive scalar transport is reduced and the advective transport becomes dominant. A comparison of Fig. 6(b) with Fig. 4 suggests that the flow rises, with lower scalar concentration, along the streamwise FGT rows, and falls, with higher scalar concentration, along the streamwise BGT rows. In the grooves, the recirculating flow helps to transport the scalar to the bottom surfaces and the side walls of the herringbone ridges. In the top region, the flow acquires the scalar from the top plane through scalar diffusion. These consecutive steps articulate the whole process of scalar transport from the top plane to the bottom surfaces and ridge surfaces. The comparison between Figs. 6(a) and 6(b) confirms the conclusion that the advective scalar transfer primarily takes effect at larger Schmidt numbers.

Figure 7 shows the advective scalar transport flux in the vertical direction $\tilde{u}_z\phi$ for $Sc = 1$ and 50 at $Re_S = 200$. The 3D iso-surfaces and 2D iso-contours of $\tilde{u}_z\phi$ are consistent with the patterns of vertical velocity $\tilde{u}_z$ shown in Fig. 4. Along the steamwise FGT rows, the values of $\tilde{u}_z\phi$ are positive, indicating an upward advective scalar flux. Along the BGT rows, the values of $\tilde{u}_z\phi$

are negative, indicating a downward advective scalar flux. At $Sc = 1$, the stronger diffusion effect reveals tubular structures in the iso surfaces that extend in the streamwise direction on each row of the herringbone ridges. At $Sc = 50$, the enhanced advection effect creates complex fine structures on the iso-surfaces. A comparison of the 2D contours suggests that at $Sc = 1$ the value of $\tilde{u}_z\phi$ in the upward flow is larger and the absolute value of $\tilde{u}_z\phi$ in the downward flow is smaller compared with the values at $Sc = 50$. This implies that the net efficiency of advective scalar transport from the top plane to the bottom region is lower at $Sc = 1$. As a result, the total scalar flux is lower.

The scalar transport from the top plane to the bottom region relies on both scalar diffusion and the flow advection induced by the herringbone structures. In nondimensional form, the diffusive and advective scalar fluxes, $\tilde{q}_{dif}(\tilde{z})$ and $\tilde{q}_{adv}(\tilde{z})$, are calculated as,

$$\tilde{q}_{dif}(\tilde{z}) = \frac{1}{Pe}\langle\frac{\partial\phi}{\partial\tilde{z}}\rangle \tag{15}$$

$$\tilde{q}_{adv}(\tilde{z}) = -\langle\tilde{u}_z\phi\rangle \tag{16}$$

where Pe is the Peclet number. The total flux $\tilde{q}_{tot}$ is the sum of $\tilde{q}_{dif}(\tilde{z})$ and $\tilde{q}_{adv}(\tilde{z})$,

$$\tilde{q}_{tot} = \frac{1}{Pe}\langle\frac{\partial\phi}{\partial\tilde{z}}\rangle(\tilde{z}) - \langle\tilde{u}_z\phi\rangle(\tilde{z}) \tag{17}$$

Both $\tilde{q}_{dif}(\tilde{z})$ and $\tilde{q}_{adv}(\tilde{z})$ are functions of the vertical coordinate $\tilde{z}$, yet the total scalar flux $\tilde{q}_{tot}$ is independent of $\tilde{z}$ in the steady state due to the conservation of scalar flux.

To quantitatively compare the scalar transport characteristics of the flows at various Sc at Re_S, Figs. 8 and 9 show the profile of the horizontally averaged scalar concentration $\langle\phi\rangle$, the gradient of scalar concentration in the vertical direction $\langle\partial\phi/\partial\tilde{z}\rangle$, and the ratio of advective scalar flux to total scalar flux $|\langle\tilde{u}_z\phi\rangle|/\tilde{q}_{tot}$ for various Sc at $Re_S = 20$ and 200, respectively. $\langle\partial\phi/\partial\tilde{z}\rangle$

quantifies the diffusive scalar transport in the vertical direction, and $|\langle\tilde{u}_z\phi\rangle|/\tilde{q}_{tot}$ represents the fraction of the advective scalar flux in the total scalar flux. For the purposes of comparison, the curves of scalar transport with pure diffusion are also included. The pure diffusion results were obtained by simulating the scalar transport in a quiescent fluid using the same numerical method. For both Re_S, the variations of $\langle\phi\rangle$, $\langle\partial\phi/\partial\tilde{z}\rangle$ and $|\langle\tilde{u}_z\phi\rangle|/\tilde{q}_{tot}$ with vertical coordinate $\tilde{z}$ demonstrate similar dependence on Sc. As Sc increases, the advection effect gets stronger, and the curves deviate more from those of pure diffusion. For a given Sc, higher Re_S leads to a stronger advection effect and more deviation amongst the curves. For pure diffusion, $\langle\phi\rangle$ is linearly dependent on $\tilde{z}$, that is, $\langle\partial\phi/\partial\tilde{z}\rangle$ is a constant above the herringbone structures and so maintains a constant scalar flux in the vertical direction. The advective scalar flux $\langle\tilde{u}_z\phi\rangle$ is zero everywhere. At nonzero Reynolds numbers, the disturbances produced by the herringbone structures cause local mixing above the ridges, which not only decreases the vertical gradient of $\langle\phi\rangle$ in the local area, but also provides an advective scalar transfer mechanism. With the increase in Sc, the advection effect becomes stronger and the gradient of $\langle\phi\rangle$ becomes smaller.

For $Re_S = 20$, as shown in Fig. 8, with the increase in Sc the curve of $\langle\phi\rangle$ becomes more vertical at about $\tilde{z} = 1.5$, and the curve of $\langle\partial\phi/\partial\tilde{z}\rangle$ curves leftward and forms a peak with the minimum $\langle\partial\phi/\partial\tilde{z}\rangle$. At the same time, the curve of $|\langle\tilde{u}_z\phi\rangle|/\tilde{q}_{tot}$ curves rightward and forms a peak with the maximum $|\langle\tilde{u}_z\phi\rangle|/\tilde{q}_{tot}$. This means that the fraction of advective scalar flux of the total scalar flux increases with Sc. At the top plane ($\tilde{z} = 3$), scalar transport occurs by pure diffusion because the vertical velocity is 0 there. When Sc increases from 1 to 50, the curve slope of $\langle\phi\rangle$, that is, the value of $\langle\partial\phi/\partial\tilde{z}\rangle$ at the top plane, also increases. This means that the total scalar flux increases with Sc as a result of enhanced advective scalar transfer. Since the passive scalar is absorbed at both the side walls of the herringbone ridges and the bottom surfaces, the curve of $\langle\phi\rangle$

is not a straight line in the grooves ($\tilde{z} < 1$) for pure diffusion. At $Re_S = 20$, the flow advection is weak in the grooves, so the curves of $\langle\phi\rangle$ and $\langle\partial\phi/\partial\tilde{z}\rangle$ do not change much with Sc when $\tilde{z} < 1$, yet the curves of $|\langle\tilde{u}_z\phi\rangle|/\tilde{q}_{tot}$ still show the enhancement of advective scalar transport in the grooves.

For $Re_S = 200$, the curves shown in Fig. 9 demonstrate a strong advection effect due to the decrease in the kinematic viscosity of the fluid – except the curve for $Sc = 1$. As shown in the figure, the curves of $\langle\phi\rangle$, $\langle\partial\phi/\partial\tilde{z}\rangle$, and $|\langle\tilde{u}_z\phi\rangle|/\tilde{q}_{tot}$ for $Sc = 1$ almost coincide with those of pure diffusion. However, when Sc increases to 10, the value of $\langle\phi\rangle$ decreases and the curve of $\langle\phi\rangle$ is almost vertical above the herringbone structures. Correspondingly, the curve of $\langle\partial\phi/\partial\tilde{z}\rangle$ has a minimum value close to 0 at about $\tilde{z} = 1.5$, and the curve of $|\langle\tilde{u}_z\phi\rangle|/\tilde{q}_{tot}$ shows a maximum value close to 1 at that point. This means that advective scalar transfer has become the dominant means of scalar transport.

As Sc increases from 10 to 50, the value of $\langle\phi\rangle$ further decreases above the herringbone structures, and the area of small $\langle\partial\phi/\partial\tilde{z}\rangle$ (close to 0) expands both upward and downward. Correspondingly, the area of large $|\langle\tilde{u}_z\phi\rangle|/\tilde{q}_{tot}$ (close to 1) also expands. The advective scalar transfer dominates in the majority of the upper flow. At the top plane, scalar transport relies on pure diffusion. As Sc increases from 1 to 50, the slope of the curve of $\langle\phi\rangle$, that is, the value of $\langle\partial\phi/\partial\tilde{z}\rangle$ at the top plane, also increases, indicating an increase in total scalar flux from the top plane to the flow. In the grooves, $\langle\phi\rangle$ smoothly decreases from a small value at ridge tips to 0 at the bottom surface for pure diffusion, and the curve slope of $\langle\phi\rangle$, that is, the value of $\langle\partial\phi/\partial\tilde{z}\rangle$ is close to 0 at the bottom surface. This suggests that only a small fraction of scalar is transported to the bottom surface through pure diffusion. At $Sc = 1$, the scalar transfer characteristics are almost the same as those for pure diffusion. When Sc increases to 10, the curve of $\langle\phi\rangle$ becomes vertical

below the ridge tips, and the value of $\langle \partial\phi/\partial\tilde{z} \rangle$ decreases toward 0. Correspondingly, the curve of $|\langle \tilde{u}_z\phi \rangle|/\tilde{q}_{tot}$ shows apparent increase in $|\langle \tilde{u}_z\phi \rangle|/\tilde{q}_{tot}$ in that area. As Sc further increases, the flow recirculation in the grooves becomes stronger, further decreasing the value of $\langle \partial\phi/\partial\tilde{z} \rangle$ and increasing the value of $|\langle \tilde{u}_z\phi \rangle|/\tilde{q}_{tot}$ below the ridge tips. At the bottom surface ($\tilde{z} = 0$), the increase in Sc leads to an increase in $\langle \partial\phi/\partial\tilde{z} \rangle$, i.e., the scalar flux transported to the bottom surface increases.

To measure the enhancement of scalar transport from the top plane to the herringbone surfaces and bottom plane, we compare the total scalar flux in the presence of herringbone structures with that of a smooth bottom plane. Scalar transport in laminar flows between smooth planes is by pure diffusion. We select two distances H_{smo} between the top and bottom smooth planes. The first, $\widetilde{H}_{smo} = 3\tilde{h}$, corresponds to the case in which the top and bottom planes are at the same positions as those of the cases with herringbone structures. The second, $\widetilde{H}_{smo} = 2\tilde{h}$, corresponds to the case in which the top plane is at the same position as that considered in this study and the bottom plane is at the tips of the herringbone structures. The nondimensional scalar fluxes between the smooth planes are calculated as,

$$\tilde{q}_{smo} = (\phi_0 - 0)/\widetilde{H}_{smo} = 1/3 \qquad \text{when} \quad \widetilde{H}_{smo} = 3\tilde{h} \tag{18}$$

$$\tilde{q}_{smo} = (\phi_0 - 0)/\widetilde{H}_{smo} = 1/2 \qquad \text{when} \quad \widetilde{H}_{smo} = 2\tilde{h} \tag{19}$$

Figure 10 shows the ratio of total scalar flux with herringbone structures to those with the smooth bottom wall $\tilde{q}_{tot}/\tilde{q}_{smo}$ versus Schmidt number Sc in logarithm scales. Compared with the smooth planes at $\widetilde{H}_{smo} = 3\tilde{h}$, the herringbone structures significantly enhance the scalar transport by reducing the transfer distance, increasing surface area, and inducing flow advection in the vertical direction. As a result, $\tilde{q}_{tot}/\tilde{q}_{smo}$ is always greater than 1, as shown in Fig. 10(a).

For pure diffusion, which is equivalent to $Re_S = 0$, $\tilde{q}_{tot}/\tilde{q}_{smo}$ denoted as $(\tilde{q}_{tot}/\tilde{q}_{smo})_{dif}$, is independent of Sc and remains at a value about 1.43. This value is determined by the distance between the top and bottom planes and the geometric parameters of the herringbone structures. For $Re_S > 0$, $\tilde{q}_{tot}/\tilde{q}_{smo}$ increases with both Sc and Re_S from the pure diffusion value. At $Re_S = 20$, the scalar transport is dominated by diffusion from $Sc = 0$ to a critical Schmidt number Sc_{crit} around 10, after which $\tilde{q}_{tot}/\tilde{q}_{smo}$ increases monotonically with Sc due to the enhancement from flow advection. It is apparent that Sc_{crit} decreases with the increase in Re_S. At $Re_S = 100$ and 200, $\tilde{q}_{tot}/\tilde{q}_{smo}$ is close to $(\tilde{q}_{tot}/\tilde{q}_{smo})_{dif}$ when $Sc = 1$. After that, $\tilde{q}_{tot}/\tilde{q}_{smo}$ increases remarkably with the increase in Sc. Note that in logarithm scale the curves appear as straight lines and the slopes are almost the same when $Sc \geq 10$ for $Re_S = 100$ and 200. This implies that the variation of $\tilde{q}_{tot}/\tilde{q}_{smo}$ follows a power law on Sc when advective scalar transport dominates, and the exponent of Sc is independent of Re_S.

For the flows considered in this study, it is found that the exponent approaches eventually to a value close to 0.4 as Sc increases. Figure 10(b) shows the enhancement of scalar transfer by the herringbone structures compared with the flow over smooth planes with $\widetilde{H}_{smo} = 2\tilde{h}$. In this comparison, the herringbone structures increase the scalar transport distance from the top plane to the herringbone surfaces and bottom planes, so $\tilde{q}_{tot}/\tilde{q}_{smo}$ becomes less than 1 for pure diffusion. However, with the increase in Sc and Re_S, the strengthened advection effect not only offsets the reduction of scalar transfer caused by increased transport distance, but also causes a significant increase in $\tilde{q}_{tot}/\tilde{q}_{smo}$. Since $\tilde{q}_{smo}$ is independent of Sc and Re_S, the enhancement of scalar transport, $\tilde{q}_{tot}/\tilde{q}_{smo}$, can be written in a unified form,

$$\tilde{q}_{tot}/\tilde{q}_{smo} = f(Re_S, Sc, \boldsymbol{\gamma}) \tag{20}$$

where $\boldsymbol{\gamma}$ is a vector of the geometric parameters, such as the distance between the two planes and the height of herringbone structures, and $f(Re_S, Sc, \boldsymbol{\gamma})$ is a function of Re_S, Sc and $\boldsymbol{\gamma}$. The variation of $\tilde{q}_{tot}/\tilde{q}_{smo}$ with Sc shown in Fig. 10 suggests that $\tilde{q}_{tot}/\tilde{q}_{smo}$ has a power law relationship with Sc, with an exponent of 0.4 when advective scalar transport takes effect. Therefore, Eqn. (20) can be further written as,

$$\tilde{q}_{tot}/\tilde{q}_{smo} = g(Re_S, \boldsymbol{\gamma})Sc^{0.4} \tag{21}$$

where $g(Re_S, \boldsymbol{\gamma})$ is a function of Re_S and $\boldsymbol{\gamma}$. For turbulent heat transfer, it has been found that the Nusselt number Nu, a nondimensional parameter characterizing the heat transfer rate, can be expressed as the Dittus-Boelter equation,[35]

$$Nu = 0.023Re^{0.8}Pr^{0.4} \tag{22}$$

In this expression, the exponent of Pr is 0.4, which is the same as that in Eq. (21).

To further explore the dependence of scalar transfer rate on Re_S and Sc, we select the data points at $Sc = 10$, 30 and 50 from Fig. 10(a) and plot $\tilde{q}_{tot}/\tilde{q}_{smo}$ versus Re_S in logarithm scale in Fig. 11. To compare with the Dittus-Boelter equation, we include $\tilde{q}_{tot}/\tilde{q}_{smo} \propto Re^{0.8}$. As shown in the figure, the curves of the three Schmidt numbers exhibit almost the same slopes at every Re_S except in the lower left region around $Re_S = 20$ and $Sc = 10$, where the scalar transport is dominated by diffusion. The curve slopes asymptotically approach the slope of $\tilde{q}_{tot}/\tilde{q}_{smo} \propto Re^{0.8}$ as Re_S increases. While the range of Re_S considered in this study is limited, it is almost certain that the dependence of scalar transport on Sc will become a power law as Re_S further increases, with the exponent close to 0.8. Once the power law relationship is reached, the expression of $\tilde{q}_{tot}/\tilde{q}_{smo}$ given in Eqn. (21) could be further decomposed as,

$$\tilde{q}_{tot}/\tilde{q}_{smo} = h(\boldsymbol{\gamma})Re_S^m Sc^{0.4} \tag{23}$$

where m is a value close to 0.8. This suggests that when Re_S is large enough, the heat and mass transfer rates also have a power law relationship with Re_S, and the effects of geometric parameters $\boldsymbol{\gamma}$, Reynolds number Re_S, and Schmidt number Sc are decoupled. The scalar transfer rate can be expressed in the general form as,

$$\tilde{q}_{tot} = f(Re_S, Sc, \boldsymbol{\gamma}) \xrightarrow{adv.\ dom} g(Re_S, \boldsymbol{\gamma}) Sc^{0.4} \xrightarrow{large\ Re_S} c(\boldsymbol{\gamma}) Re_S^m Sc^{0.4} \tag{24}$$

where $m \approx 0.8$. ('adv. dom.' indicates the advection-dominant regime).

If the scalar transfer rates from the numerical simulations are fitted within the finite range of Re_S to the power law relationship with the least square method, we obtain,

$$\tilde{q}_{tot} = c(\boldsymbol{\gamma}) Re_S^{0.42} Sc^{0.4} \tag{25}$$

The exponent of Re_S is 0.42, smaller than that in the Dittus-Boelter equation.

The Peclet number, which is defined as the product of the Reynolds and Schmidt numbers, is another important nondimensional parameter characterizing scalar transport. Figure 12 shows the enhancement of scalar transfer $\tilde{q}_{tot}/\tilde{q}_{smo}$ versus Peclet number Pe for the two $\widetilde{H}_{smo}$. As shown in the figure, all the curves demonstrate a power law relationship with Pe in the logarithm scale when Pe increases above a critical value around 200. The curves at different values of Re_S group together and form a dense cluster of curves. The curve slopes are roughly the same as that of $Pe^{0.4}$. If we use Eqn. (24) to approximate the scalar transport rate in the range considered in this study, the expression can be rearranged as

$$\tilde{q}_{tot} = c(\boldsymbol{\gamma}) Re_S^{0.02} Pe^{0.4} \tag{26}$$

The term $Re_S^{0.02}$, that is, the Reynolds number effect, causes deviation among the curves at different Re_S values, but for the Re_S in this study, $Re_S^{0.02} \approx 1$, the curves are close. Therefore, the scalar transport rate can be roughly estimated by

$$\tilde{q}_{tot} = c(\boldsymbol{\gamma}) Pe^{0.4} \tag{27}$$

when Re_S is not very large. This simplified expression will significantly simplify the estimation of heat and mass transfer rate for industrial applications.

The mechanisms and conclusions presented here also apply to cases with heat and mass transfer from the bottom surface to the top plane, with a simple conversion.

5. Conclusion

Focusing a simple shear flow over staggered herringbone structures, we have identified the mechanisms of heat and mass transfer induced by the transverse flow induced by the repetitive herringbone structures. Proposing that the herringbone structures enhance heat and mass transfer through lateral convection, we identify the basic flow characteristics induced by the structures, and elaborate the power-law dependence of heat or mass transfer rate on Schmidt and Reynolds numbers. This work provides a new idea for the design and optimization of microfluidic systems involving heat and mass transfer.

Through high-fidelity numerical simulation, two basic flow motions are identified, which provide the fundamental mechanisms for heat and mass transfer through flow advection. The first is a spiral flow oscillation between the top plane and the herringbone structures, which transports heat and mass from the top plane (or bulk flow) to the regions around herringbone tips. The second is flow recirculation in the grooves between the ridges, which transports heat and mass from the

areas around the herringbone tips to the side walls of herringbone ridges and the bottom surfaces. These two basic flow motions couple together to form a complex transport mechanism.

When advective heat and mass transfer takes effect at relatively larger Reynolds and Schmidt numbers, the dependence of the total transfer rate on the Schmidt number follows a power law; the exponent is the same as that in the well-known Dittus-Boelter equation for turbulent heat transfer. As the Reynolds number increases, the dependence of total transfer rate on the Reynolds number also approaches a power law, and the exponent is close to that in the Dittus-Boelter equation. When the power law on Reynolds number is reached, the dependence on geometric parameters, Reynolds numbers, and Schmidt numbers can be decoupled. This discovery will facilitate the development of physics-based models for a wide range of fundamental research and industrial applications.

References

1. C.-M. Ho, and Y.-C. Tai, "Micro-electro-mechanical-systems (MEMS) and fluid flows," Annual Review of Fluid Mechanics **30**, 579 (1998).
2. H. A. Stone, A. D. Stroock, and A. Ajdari, "Engineering flows in small devices: microfluidics toward a lab-on-a-chip," Annu. Rev. Fluid Mech. **36**, 381 (2004).
3. D. T. Chiu, A. J. deMello, D. Di Carlo, P. S. Doyle, C. Hansen, R. M. Maceiczyk, and R. C. R. Wootton, "Small but perfectly formed? Successes, challenges, and opportunities for microfluidics in the chemical and biological sciences," Chem **2**, 201 (2017).
4. A. D. Stroock, S. K. W. Dertinger, A. Ajdari, I. Mezić, H. A. Stone, and G. M. Whitesides, "Chaotic mixer for microchannels," Science **295**, 647 (2002).
5. J. M. Ottino, and S. Wiggins, "Designing optimal micromixers," Science **305**, 485 (2004).
6. J. T. Yang, K. J. Huang, and Y. C. Lin, "Geometric effects on fluid mixing in passive grooved micromixers," Lab Chip **5**, 1140 (2005).
7. J. Aubin, D. F. Fletcher, and C. Xuereb, "Design of micromixers using CFD modelling," Chemical Engineering Science **60**, 2503 (2005).
8. D. G. Hassell, and W. B. Zimmerman, "Investigation of the convective motion through a staggered herringbone micromixer at low Reynolds number flow," Chemical Engineering Science **61**, 2977 (2006).
9. S. Hardt, K. S. Drese, V. Hessel, and F. Schönfeld, "Passive micromixers for applications in the microreactor and μTAS fields," Microfluidics and Nanofluidics **1**, 108 (2005).
10. S. L. Stott, C.-H. Hsu, D. I. Tsukrov, M. Yu, D. T. Miyamoto, B. A. Waltman, S. M. Rothenberg, A. M. Shah, M. E. Smas, G. K. Korir, F. P. Floyd, A. J. Gilman, J. B. Lord, D. Winokur, S. Springer, D. Irimia, S. Nagrath, L. V. Sequist, R. J. Lee, K. J. Isselbacher, S. Maheswaran, D. A. Haber, and M. Toner, "Isolation of

circulating tumor cells using a microvortex-generating herringbone-chip," Proceedings of the National Academy of Sciences **107**, 18392 (2010).
11. M. A. Ansari, and K.-Y. Kim, "Shape optimization of a micromixer with staggered herringbone groove," Chemical Engineering Science **62**, 6687 (2007).
12. C. A. Cortes-Quiroz, M. Zangeneh, and A. Goto, "On multi-objective optimization of geometry of staggered herringbone micromixer," Microfluidics and nanofluidics **7**, 29 (2009).
13. S. Hossain, A. Husain, and K.-Y. Kim, "Optimization of micromixer with staggered herringbone grooves on top and bottom walls," Engineering Applications of Computational Fluid Mechanics **5**, 506 (2011).
14. P. B. Howell, Jr., D. R. Mott, S. Fertig, C. R. Kaplan, J. P. Golden, E. S. Oran, and F. S. Ligler, "A microfluidic mixer with grooves placed on the top and bottom of the channel," Lab Chip **5**, 524 (2005).
15. D. Lin, F. He, Y. Liao, J. Lin, C. Liu, J. Song, and Y. Cheng, "Three-dimensional staggered herringbone mixer fabricated by femtosecond laser direct writing," Journal of Optics **15**, 025601 (2013).
16. D. Gobby, P. Angeli, and A. Gavriilidis, "Mixing characteristics of T-type microfluidic mixers," Journal of Micromechanics and Microengineering **11**, 126 (2001).
17. F. Yang, M. Alwazzan, W. Li, and C. Li, "Single- and two-phase thermal transport in microchannels with embedded staggered herringbone mixers," Journal of Microelectromechanical Systems **23**, 1346 (2014).
18. J. Marschewski, R. Brechbühler, S. Jung, P. Ruch, B. Michel, and D. Poulikakos, "Significant heat transfer enhancement in microchannels with herringbone-inspired microstructures," International Journal of Heat and Mass Transfer **95**, 755 (2016).
19. M. Bisht, S. Haeri, and D. V. Patil, "Fluid flow in wall-driven enclosures with corrugated bottom," Computers & Fluids **152**, 1 (2017).
20. Y. H. Qian, D. D'Humières, and P. Lallemand, "Lattice BGK models for Navier-Stokes equation," Europhysics Letters (EPL) **17**, 479 (1992).
21. S. Chen, and G. D. Doolen, "Lattice Boltzmann method for fluid flows," Annual review of fluid mechanics **30**, 329 (1998).
22. Y. Wang, J. Brasseur, G. Banco, A. Webb, A. Ailiani, and T. Neuberger, "*Development of a lattice-Boltzmann method for multiscale transport and absorption with application to intestinal function,"* in S. De et al., Computational Modeling in Biomecchanics, Springer, 2010, 69-96.
23. P. Lallemand, and L.-S. Luo, "Lattice Boltzmann method for moving boundaries," Journal of Computational Physics **184**, 406 (2003).
24. A. J. C. Ladd, "Numerical simulations of particulate suspensions via a discretized Boltzmann equation. Part 1. Theoretical foundation," Journal of Fluid Mechanics **271**, 285 (1994).
25. P. Lallemand, and L.-S. Luo, "Theory of the lattice Boltzmann method: Dispersion, dissipation, isotropy, Galilean invariance, and stability," Physical review E **61**, 6546 (2000).
26. P. Lallemand, and L.-S. Luo, "Theory of the lattice Boltzmann method: Acoustic and thermal properties in two and three dimensions," Physical review E **68**, 036706 (2003).
27. D. Frenkel, and M. H. Ernst, "Simulation of diffusion in a two-dimensional lattice-gas cellular automaton: A test of mode-coupling theory," Physical Review Letters **63**, 2165 (1989).
28. C. P. Lowe, and D. Frenkel, "The super long-time decay of velocity fluctuations in a two-dimensional fluid," Physica A: Statistical Mechanics and its Applications **220**, 251 (1995).
29. R. M. H. Merks, A. G. Hoekstra, and P. M. A. Sloot, "The Moment propagation method for advection–diffusion in the lattice Boltzmann mmethod: Validation and Péclet number limits," Journal of Computational Physics **183**, 563 (2002).
30. Y. Wang, J. G. Brasseur, G. G. Banco, A. G. Webb, A. C. Ailiani, and T. Neuberger, "A multiscale lattice Boltzmann model of macro-to micro-scale transport, with applications to gut function," Philosophical Transactions of the Royal Society A: Mathematical, Physical and Engineering Sciences **368**, 2863 (2010).
31. Y. Wang, and J. G. Brasseur, "Three-dimensional mechanisms of macro-to-micro-scale transport and absorption enhancement by gut villi motions," Physical Review E **95**, 062412 (2017).

32. Y. Wang, and J. G. Brasseur, "Enhancement of mass transfer from particles by local shear-rate and correlations with application to drug dissolution," AIChE Journal **65**, e16617 (2019).
33. S. Popinet, "Gerris: a tree-based adaptive solver for the incompressible Euler equations in complex geometries," Journal of Computational Physics **190**, 572 (2003).
34. S. Popinet, "An accurate adaptive solver for surface-tension-driven interfacial flows," Journal of Computational Physics **228**, 5838 (2009).
35. H. W. McAdams, *Heat Transmission* (McGraw-Hill, 1954).

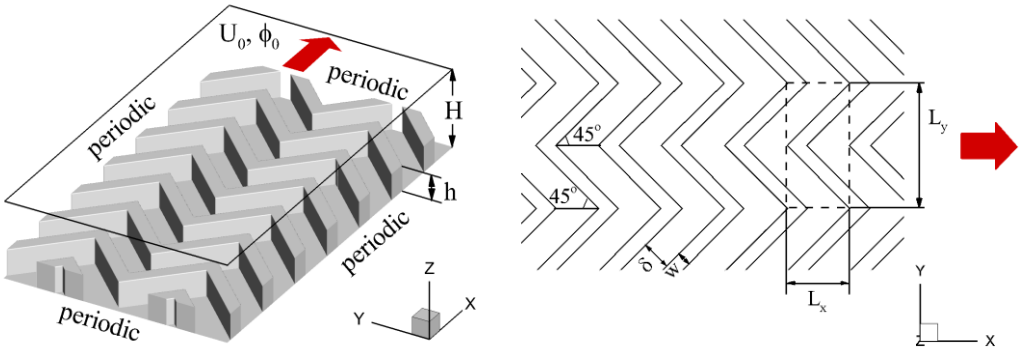

(a) (b)

Fig. 1. Physical model of heat and mass transfer in a simple shear flow with herringbone structures on bottom wall. (a) 3D view, and (b) top view. The dashed rectangle indicates the domain of numerical simulation.

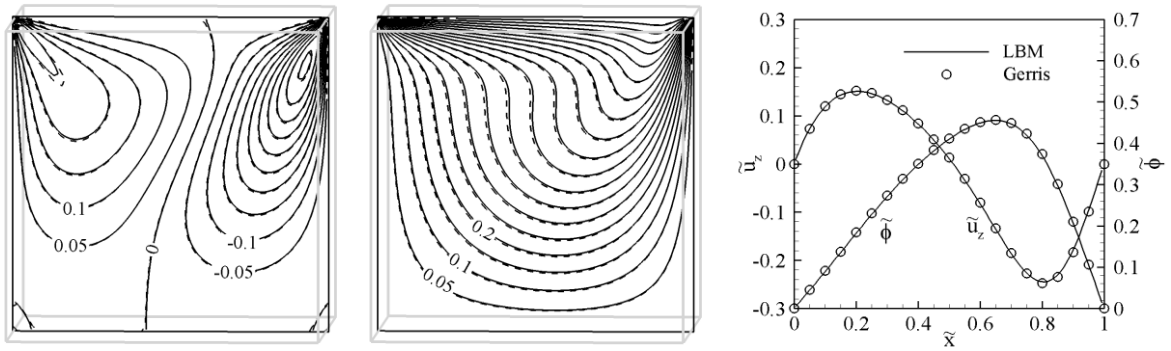

Fig. 2. Vertical velocity ($\tilde{u}_z$) and temperature ($\tilde{\phi}$) using the present LBM method (solid lines) and the open-source code Gerris (dashed lines). (a) iso-contours of $\tilde{u}_z$ on the middle *xz* plane, (b) iso-contours of $\tilde{\phi}$ on the middle *xz* plane, and (c) profiles of $\tilde{u}_z$ and $\tilde{\phi}$ along the central streamwise axis.

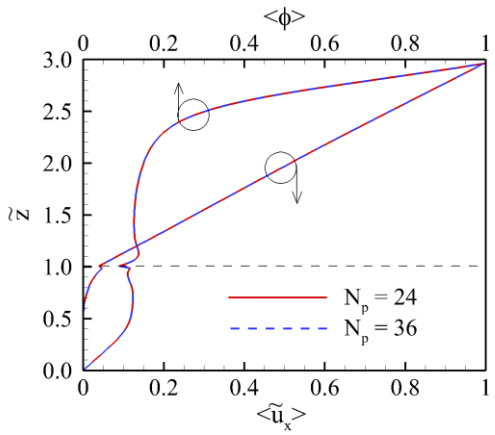

Fig. 3. Effect of grid resolution on horizontally averaged streamwise velocity $\langle \tilde{u}_x \rangle$ and scalar concentration $\langle \phi \rangle$ at $Re_S = 200$ and $Sc = 50$. N_p is the number of grid points over one herringbone ridge.

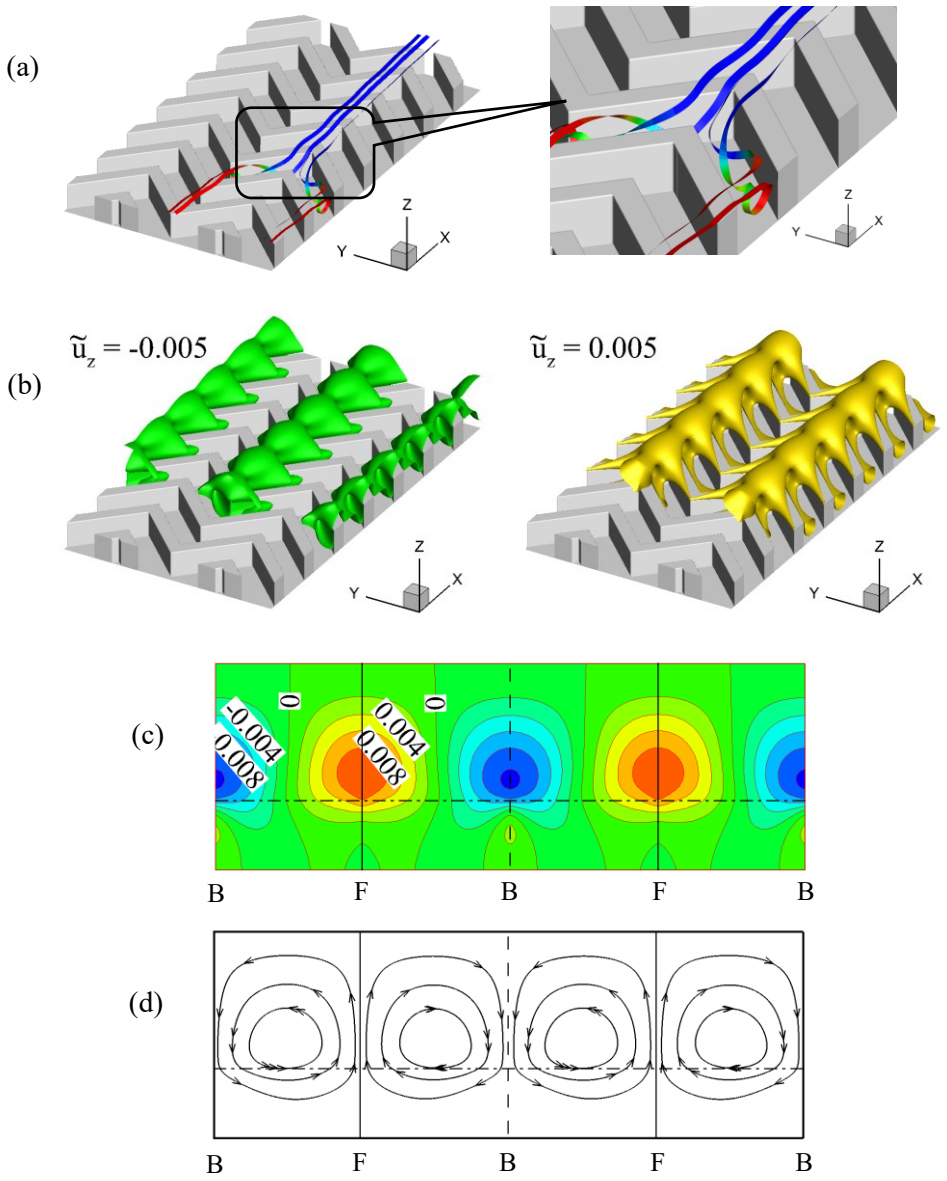

Fig. 4. Flow patterns induced by herringbone structures in a simple shear flow at $Re_S = 200$. (a) typical streamtraces trapped in the grooves of herringbone structures, (b) iso-surfaces of vertical velocity at $\tilde{u}_z = \pm 0.005$, (c) 2D contours of vertical velocity averaged over streamwise coordinate $\langle \tilde{u}_z \rangle_x$, and (d) streamline patterns based on the streamwise averaged velocity components $\langle \tilde{u}_y \rangle_x$ and $\langle \tilde{u}_z \rangle_x$ on a cross section. Letters B and F in (c) and (d) indicate the positions of backward and forward connecting points of the grooves.

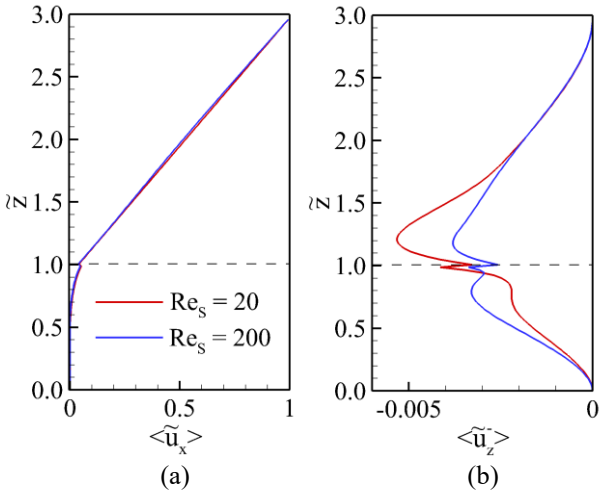

Fig. 5. Profiles of horizontally averaged velocity components. (a) streamwise velocity $\langle \tilde{u}_x \rangle$, and (b) effective downward velocity $\langle \tilde{u}_z^- \rangle$. The horizontal dashed line indicates the top of the herringbone ridges.

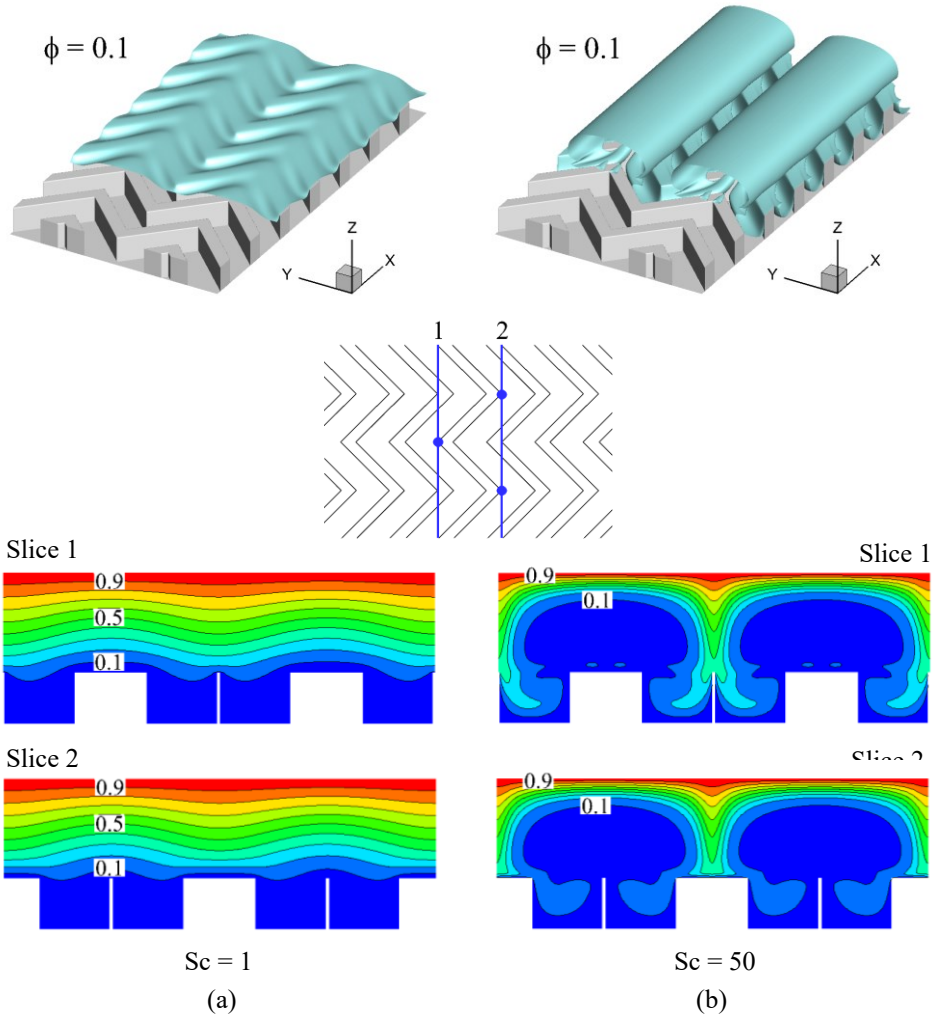

Fig. 6. Patterns of scalar concentration ϕ at $Re_S = 200$. (a) $Sc = 1$, and (b) $Sc = 50$. The sketch shows cross sections through the backward and forward connecting points of the grooves.

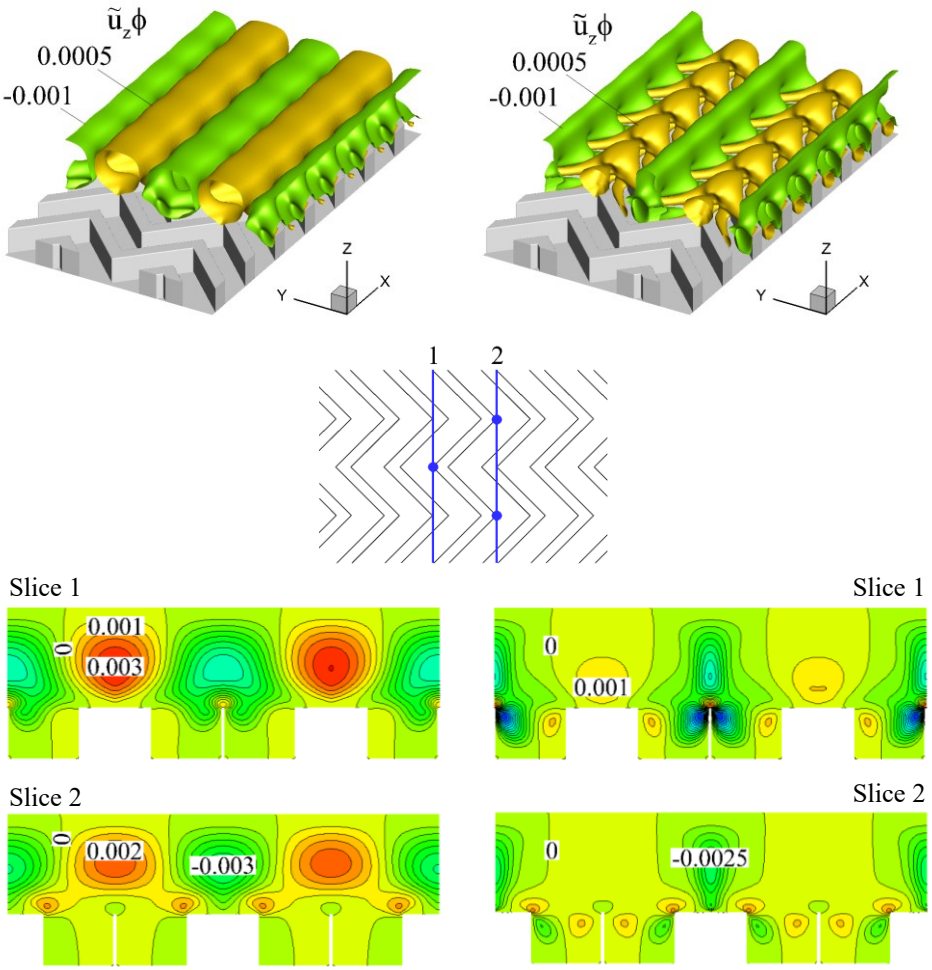

Fig. 7. Patterns of advective scalar flux in vertical direction $\tilde{u}_z\phi$ at $Re_S = 200$. (a) $Sc = 1$, and (b) $Sc = 50$. The slices are at the cross sections through the backward and forward connecting points of the grooves as shown in the sketch.

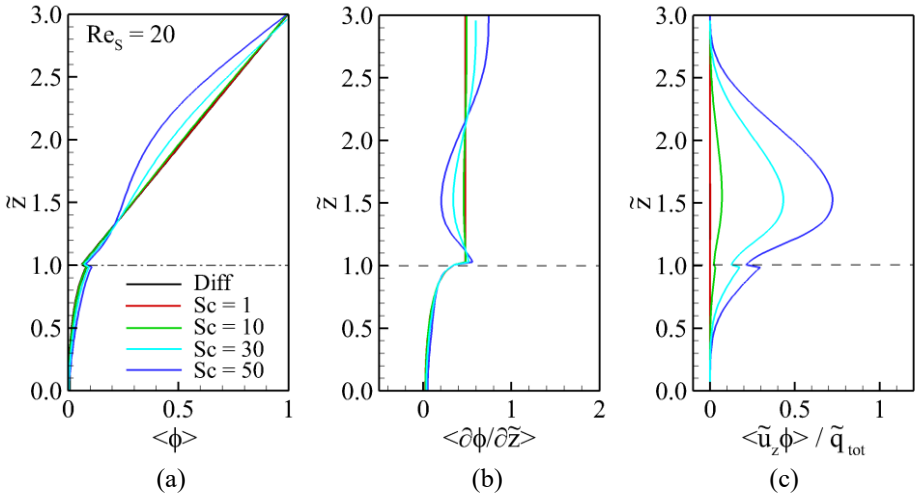

Fig. 8. Profiles of (a) horizontally averaged scalar concentration $\langle\phi\rangle$, (b) vertical gradient of scalar concentration $\langle\partial\phi/\partial\tilde{z}\rangle$, and (c) ratio of advective scalar flux to total scalar flux $|\langle\tilde{u}_z\phi\rangle|/\tilde{q}_{tot}$ at $Re_S = 20$.

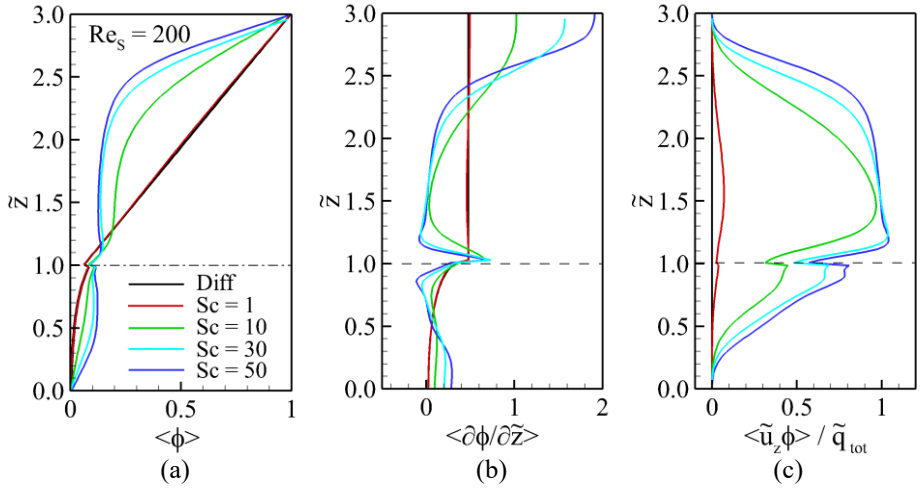

Fig. 9. Profiles of (a) horizontally averaged scalar concentration $\langle\phi\rangle$, (b) vertical gradient of scalar concentration $\langle\partial\phi/\partial\tilde{z}\rangle$, and (c) ratio of advective scalar flux to total scalar flux $|\langle\tilde{u}_z\phi\rangle|/\tilde{q}_{tot}$ at $Re_S = 200$.

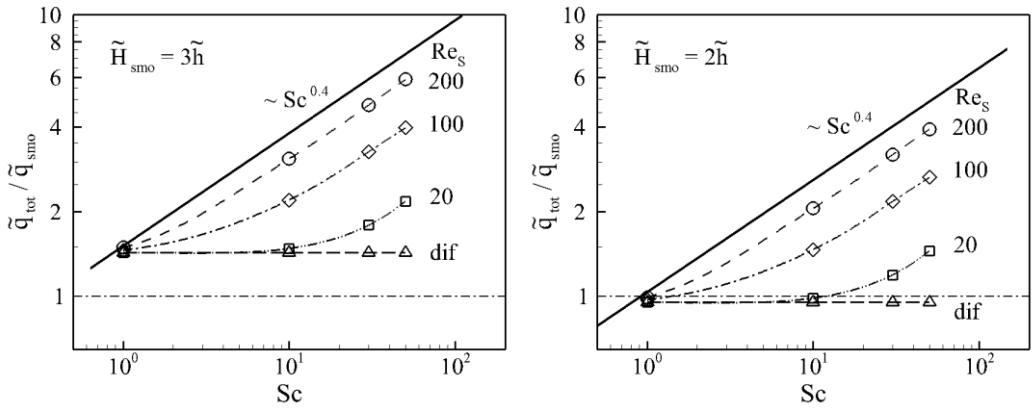

Fig. 10. Ratio of total scalar flux with herringbone structures to that with smooth bottom wall versus Schmidt number. (a) $\tilde{H}_{smo} = 3\tilde{h}$, and (b) $\tilde{H}_{smo} = 2\tilde{h}$. 'dif' indicates pure diffusion cases.

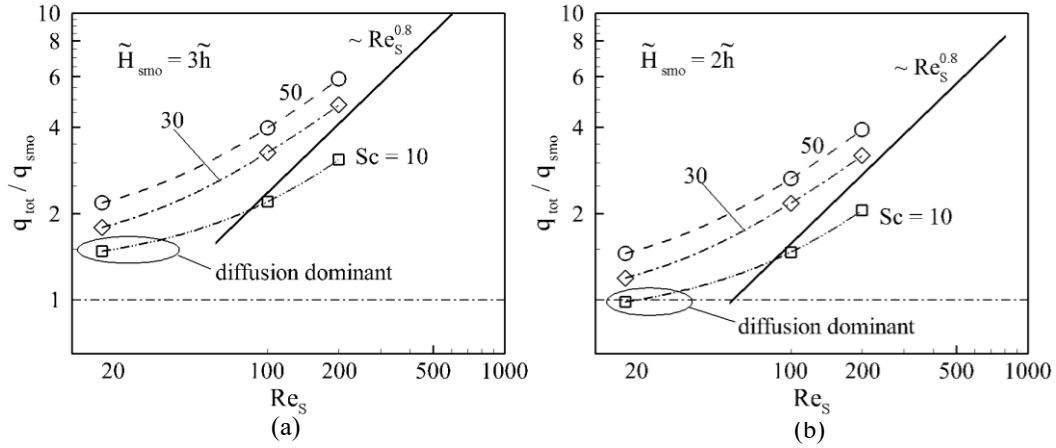

Fig. 11. Ratio of total scalar flux with herringbone structures to that with smooth bottom wall versus Reynolds number. (a) $\tilde{H}_{smo} = 3\tilde{h}$, and (b) $\tilde{H}_{smo} = 2\tilde{h}$.

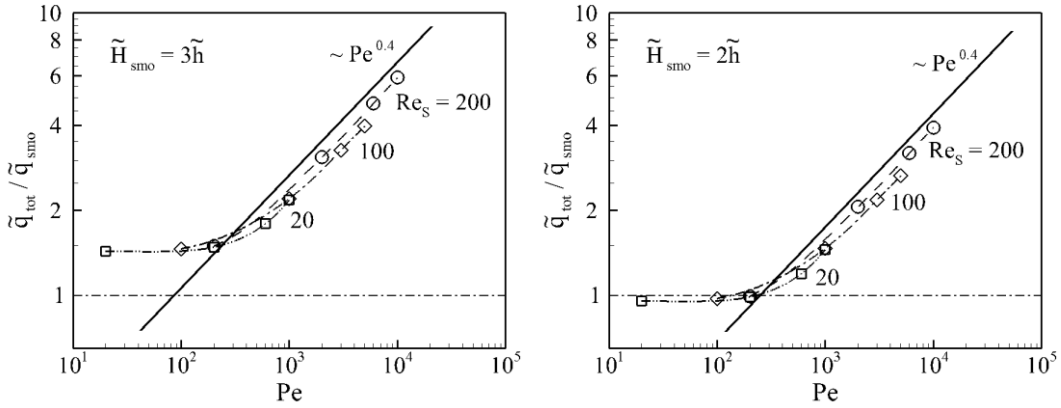

Fig. 12. Ratio of total scalar transport flux with herringbone structures to that with smooth bottom wall versus Peclet number. (a) $\widetilde{H}_{smo} = 3\tilde{h}$, and (b) $\widetilde{H}_{smo} = 2\tilde{h}$.